AGU PUBLICATIONS

JGR

Journal of Geophysical Research: Solid Earth

RESEARCH ARTICLE

10.1002/2013JB010820

Key Points:
- A V_p model up to 25 km depth is obtained for the Island of Hawaii
- A V_p/V_s model with comparative resolution as the V_p model is available
- An earthquake catalog based on 3-D velocity model and waveform data is produced

Supporting Information:
- Readme
- Catalog S1
- Catalog S2
- Catalog S3

Correspondence to:
G. Lin,
glin@rsmas.miami.edu

Citation:
Lin, G., P. M. Shearer, R. S. Matoza, P. G. Okubo, and F. Amelung (2014), Three-dimensional seismic velocity structure of Mauna Loa and Kilauea volcanoes in Hawaii from local seismic tomography, *J. Geophys. Res. Solid Earth*, *119*, doi:10.1002/2013JB010820.

Received 4 NOV 2013
Accepted 6 MAY 2014
Accepted article online 9 MAY 2014

Three-dimensional seismic velocity structure of Mauna Loa and Kilauea volcanoes in Hawaii from local seismic tomography

Guoqing Lin[1], Peter M. Shearer[2], Robin S. Matoza[2], Paul G. Okubo[3], and Falk Amelung[1]

[1]Division of Marine Geology and Geophysics, Rosenstiel School of Marine and Atmospheric Science, University of Miami, Miami, Florida, USA, [2]Institute of Geophysics and Planetary Physics, Scripps Institution of Oceanography, University of California, San Diego, California, USA, [3]Hawaiian Volcano Observatory, U.S. Geological Survey, Hawaii Volcanoes National Park, Hawaii National Park, Hawaii, USA

Abstract We present a new three-dimensional seismic velocity model of the crustal and upper mantle structure for Mauna Loa and Kilauea volcanoes in Hawaii. Our model is derived from the first-arrival times of the compressional and shear waves from about 53,000 events on and near the Island of Hawaii between 1992 and 2009 recorded by the Hawaiian Volcano Observatory stations. The V_p model generally agrees with previous studies, showing high-velocity anomalies near the calderas and rift zones and low-velocity anomalies in the fault systems. The most significant difference from previous models is in V_p/V_s structure. The high-V_p and high-V_p/V_s anomalies below Mauna Loa caldera are interpreted as mafic magmatic cumulates. The observed low-V_p and high-V_p/V_s bodies in the Kaoiki seismic zone between 5 and 15 km depth are attributed to the underlying volcaniclastic sediments. The high-V_p and moderate- to low-V_p/V_s anomalies beneath Kilauea caldera can be explained by a combination of different mafic compositions, likely to be olivine-rich gabbro and dunite. The systematically low-V_p and low-V_p/V_s bodies in the southeast flank of Kilauea may be caused by the presence of volatiles. Another difference between this study and previous ones is the improved V_p model resolution in deeper layers, owing to the inclusion of events with large epicentral distances. The new velocity model is used to relocate the seismicity of Mauna Loa and Kilauea for improved absolute locations and ultimately to develop a high-precision earthquake catalog using waveform cross-correlation data.

1. Introduction

Hawaii is one of the most seismically active regions in the world and has been serving as a natural laboratory for studying the interactions between seismic and magmatic processes for the past few decades [e.g., *Swanson et al.*, 1976; *Lipman et al.*, 1985; *Hill and Zucca*, 1987; *Rubin et al.*, 1998; *Cayol et al.*, 2000; *Hill et al.*, 2002; *Amelung et al.*, 2007; *Brooks et al.*, 2008]. The U.S. Geological Survey Hawaiian Volcano Observatory (HVO) operates an extensive seismic network (pink triangles in Figure 1) to measure and study the ongoing activity on the Island of Hawaii. Digital seismic data became available starting in 1986, including catalog data, phase picks and waveforms. This abundant data set forms an invaluable resource for studying seismicity and Earth structure in an area with high rates of tectonic and volcanic activity.

Spatial structural variations associated with volcanic activity are often imaged by tomographic inversion. Previous studies have applied different approaches using the HVO and/or temporary seismic data to study crust and upper mantle velocity structure under Mauna Loa and Kilauea volcanoes, where the seismicity is most densely distributed on the island. Refraction studies initially helped to resolve crustal structure [e.g., *Ryall and Bennett*, 1968; *Hill*, 1969]. The first three-dimensional (3-D) seismic velocity model for Kilauea was obtained by inverting teleseismic data [*Ellsworth and Koyanagi*, 1977] and was followed by numerous local tomographic studies [e.g., *Thurber*, 1984; *Rowan and Clayton*, 1993; *Okubo et al.*, 1997; *Dawson et al.*, 1999; *Haslinger et al.*, 2001; *Hansen et al.*, 2004; *Monteiller et al.*, 2005; *Park et al.*, 2007; *Got et al.*, 2008; *Park et al.*, 2009; *Syracuse et al.*, 2010]. The majority of these studies focus on the compressional (*P*) wave velocity structure near Kilauea volcano. A common feature of these previous models is high-*P* velocity anomalies at intermediate depths (5–10 km) below the volcano calderas and rift zones. Several studies also observe low-velocity zones at more shallow depths (2–4 km) within the calderas and rift zones, which have been attributed to magma bodies [e.g., *Thurber*, 1984, 1987; *Rowan and Clayton*, 1993; *Dawson et al.*, 1999;

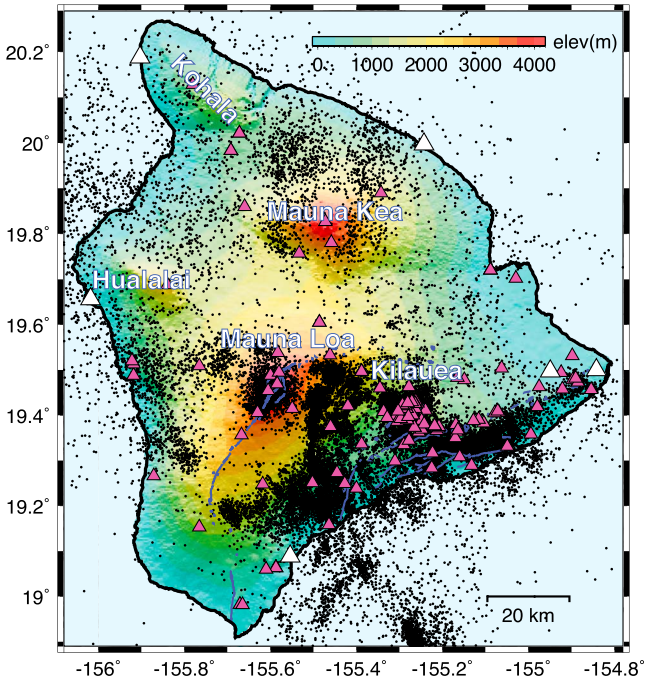

Figure 1. Seismicity (black dots) between 1992 and 2009 recorded by the HVO (pink triangles) and Pacific Tsunami Warning Center (PTWC) (white triangles) seismic stations. We only plot events with both phase picks and waveform data that are used in this study. Blue lines denote surface traces of faults. Five volcanoes from the north to the south of the Island are Kohala, Mauna Kea, Hualalai, Mauna Loa, and Kilauea. The background is the 50 m topography from the Hawaiian multibeam bathymetry synthesis (http://www.soest.hawaii.edu/hmrg/multibeam).

Park et al., 2007, 2009]. Greater constraints can be provided by a combination of V_p and V_p/V_s information on the composition of rocks, the presence of cracks, the degree of pore fluid saturation, and other properties. Due to the smaller number of *S* picks in the seismic catalogs, only a few studies of V_p/V_s models have been conducted along with V_p models. There are two V_p/V_s models available so far, one for Kilauea caldera [*Dawson et al.*, 1999] and another for its east rift zone [*Hansen et al.*, 2004].

In this study, we present a new 3-D velocity model for the crust and upper mantle structure of the entire Island of Hawaii (focusing mainly on Mauna Loa and Kilauea volcanoes) based on arrival time data recorded by the HVO and the Pacific Tsunami Warning Center (PTWC) stations. The application of the composite event method [*Lin et al.*, 2007b] enables the resolvability of both V_p and V_p/V_s models. Our V_p model not only generally agrees with previous studies but also shows some different features. Our V_p/V_s model is dominated by low values at shallow depths with limited resolution and high ratios between 6 and 9 km depth. We also produce and make available a new earthquake location catalog based on the 3-D velocity model and waveform cross correlation (http://www.rsmas.miami.edu/users/glin/Hawaii.html).

2. Data Processing

The data source for our tomographic inversions is the first-arrival times of compressional and shear waves from about 53,000 events on and near the Island of Hawaii between 1992 and 2009 recorded by the HVO and PTWC stations. Most of these events are above magnitude 1.0, with over 1.6 million first arrivals picked by analysts. There are about 80,000 more events with only waveform data (i.e., no phase picks available), which are not used in this study. Figure 1 shows the event and station distribution used here. The most seismically active regions are the Mauna Loa and Kilauea calderas and their rift zones.

In order to take advantage of the vast majority of the available picks and to improve model resolution, especially in the V_p/V_s model, we apply the recent "composite event" selection method presented by *Lin et al.* [2007b]. The idea of this approach is similar to the summary ray method of *Dziewonski* [1984] and the grid optimization approach of *Spakman and Bijwaard* [2001]. It exploits the fact that travel-time residuals (the difference between the observed and predicted arrival times) have both random picking errors and coherent signal from 3-D velocity structure. The effect of 3-D velocity structure will be nearly the same among nearby events. Thus, we can reduce the effect of random picking error for these events by averaging their residuals. We do this by creating composite events from individual events with the greatest numbers of contributing picks from nearby events within a given distance (1 and 1.5 km for different areas in this study). The composite travel times are the sum of two parts, the theoretical travel times calculated from a one-dimensional (1-D) velocity model and the source-specific station terms (SSST), which are the average travel time residuals of all the nearby events

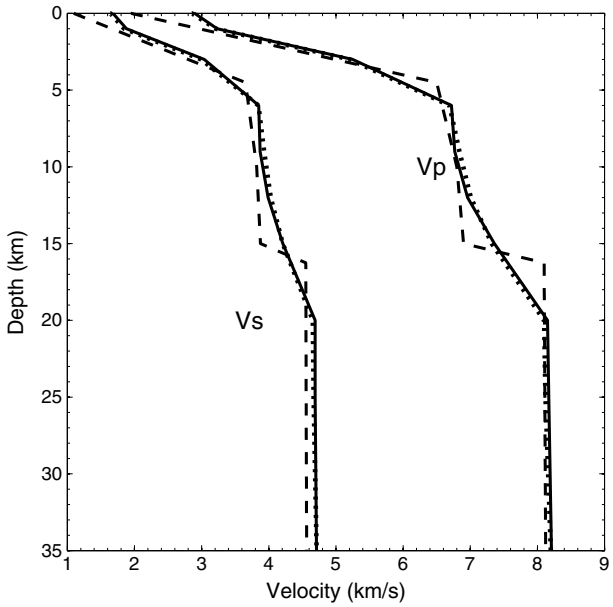

Figure 2. The 1-D velocity model used for the composite pick calculation and the 3-D tomographic inversion (solid lines), modified from *Klein* [1981] (dashed lines). Dotted lines show the layer-average model of the final 3-D inversion.

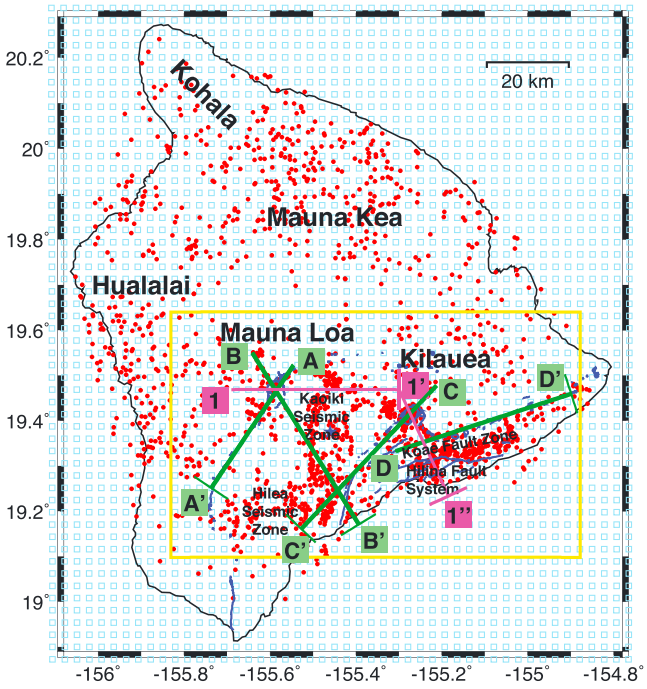

Figure 3. The composite events (red dots) and grid nodes (blue squares) used in the 3-D tomographic inversions. The yellow box encloses the area of interest in this paper. The straight lines, A-A′, B-B′, C-C′, D-D′, and 1-1′-1″, represent the depth profiles for the following cross-section views. Small bar at the end of each profile shows ±5 km width for the seismicity projection in Figure 8.

recorded by each station. In this study we make use of a modified 1-D linear gradient crustal model for south Hawaii by *Klein* [1981] (Figure 2). During this averaging process, the random picking errors can be reduced. The composite event location is assigned to the centroid of all the contributing nearby event locations.

The advantages of using composite events rather than single master events are that (1) the random picking error is reduced by averaging picks from many nearby events and (2) the maximum possible number of stations can be included for each event, which is particularly valuable for maximizing the number of *S* picks. After applying the composite event method, we obtained 1,817 composite events consisting of 64,863 *P* and 25,438 *S* wave picks. The average number of contributing picks from nearby events for each composite pick is 32. If we assume Gaussian noise, this averaging process results in an 82% reduction in random picking errors. For the HVO phase database, the number of *S* picks is about 20% that of the *P* picks. If the traditional master event selection method was applied, the V_p/V_s model would be unresolvable given our event selection criteria. These composite events and picks are the inputs to the tomographic inversions. The epicenters of the composite events are shown by the red dots in Figure 3. Because of the sparseness of seismicity on the north and west sides of the island, we focus our interest in this paper on the seismically active areas of Mauna Loa and Kilauea. Therefore, tomographic results are only shown for these two volcanoes (enclosed by the yellow box in Figure 3), although we inverted the 3-D velocity model for the entire Island.

3. Tomographic Inversion Approach

In this study, we apply the simul2000 computer program [*Thurber*, 1983,

1993; *Eberhart-Phillips*, 1990; *Thurber and Eberhart-Phillips*, 1999] to invert for both V_p and V_p/V_s models. The simul2000 algorithm is one of the most widely used approaches for local earthquake tomography. It is a damped least squares, full matrix inversion method intended for use with local earthquakes and controlled sources. During the inversion, the residuals of the *P* wave and *S-P* times are inverted for V_p, V_p/V_s variations and earthquake locations, as shown in the following equations:

$$T_{ij} = \int_{\text{source}}^{\text{receiver}} u, \mathrm{d}s \tag{1}$$

$$r_{ij}^{p} = \frac{\partial T_{ij}}{\partial x}\Delta x + \frac{\partial T_{ij}}{\partial y}\Delta y + \frac{\partial T_{ij}}{\partial z}\Delta z + \Delta\tau_i + \int_{ij} \delta u^{p}(x,y,z)\mathrm{d}s \tag{2}$$

$$r_{ij}^{s-p} = \int_{ij} \frac{\delta(V_p/V_s)}{V_p}\mathrm{d}s \tag{3}$$

where T_{ij} is the body wave travel time from an event i to a seismic station j, r_{ij}^{p} is the P wave arrival time residual and r_{ij}^{s-p} is the $S-P$ residual, respectively, (x, y, z) is the earthquake location coordinate, τ_i is the event origin time, u is the slowness ($= 1/V$), and ds is the raypath segment. The direct determination of the V_p/V_s structure using $S-P$ times is more robust than simply taking the ratio of the 3-D V_p and V_s models for body wave tomography [*Eberhart-Phillips*, 1990]. The simul2000 code uses a combination of parameter separation [*Pavlis and Booker*, 1980; *Spencer and Gubbins*, 1980] and damped least squares inversion to solve for model perturbations. The appropriate damping parameters are usually selected by using a data misfit versus model variance trade-off analysis. The resolution and covariance matrices are calculated in order to estimate the resolution of the model and the uncertainties in the model parameters. An advantage of the simul2000 algorithm is that the ray tracing is done with regard to station elevation so that the effect of topography can be taken into account [*Evans et al.*, 1994]. It has been shown that a layer of unmodeled nodes a short distance above the highest-elevation stations is helpful in situations with large topographic relief and shallow earthquakes [*Dawson et al.*, 1992]. In our study, the highest-elevation station is near Mauna Loa summit at 4 km above sea level (asl) and the unmodeled node is placed at 4.5 km asl in our inversion.

4. Velocity Model Parameterization

Our model is represented by a uniform 3 km horizontal grid (blue squares in Figure 3). The vertical nodes are positioned at −1, 1, 3, 6, 9, 12, 15, 20, 25, and 35 km depth. Note that in this study all depths are relative to mean sea level. We start our inversion with the same 1-D velocity model used for the composite pick calculation. The constant starting V_p/V_s ratio of 1.74 for the inversion gives the best fit among different tested values between 1.68 and 1.79. Damping parameters are applied to stabilize the inversion and are selected by running a series of single-iteration inversions with a large range of values and plotting the data variance versus model variance trade-off curves [e.g., *Eberhart-Phillips*, 1986, 1993]. We explored a wide range of damping to make sure that we looked at the entire trade-off curve, instead of a portion of it. Similar to the approach in *Lin et al.* [2007b], we first chose damping for V_p with a tradeoff curve while holding V_p/V_s damping fixed at a large value so that the effect of the *S* data would be as small as possible. We chose 200 as the simul2000 damping value for V_p, which produced a good compromise between data misfits and model variances. We then chose damping for V_p/V_s while holding V_p damping fixed at 200. The value we use in our tomographic inversion is 80 (Figure 4a). In order to verify that 200 is an appropriate damping value for V_p, we ran another series of single iterations with a range of V_p damping values while keeping V_p/V_s damping at 80. This trade-off curve is shown in Figure 4b. During the tomographic inversion, we did not invert for station corrections as an additional model parameter to avoid trade-offs between the model parameters and to avoid projecting resolvable shallow velocity structure into the station corrections. After we obtained the final velocity model, the root-mean-square of the arrival time residuals for the composite events is reduced by 68% from 0.40 s to 0.13 s (Figure 5).

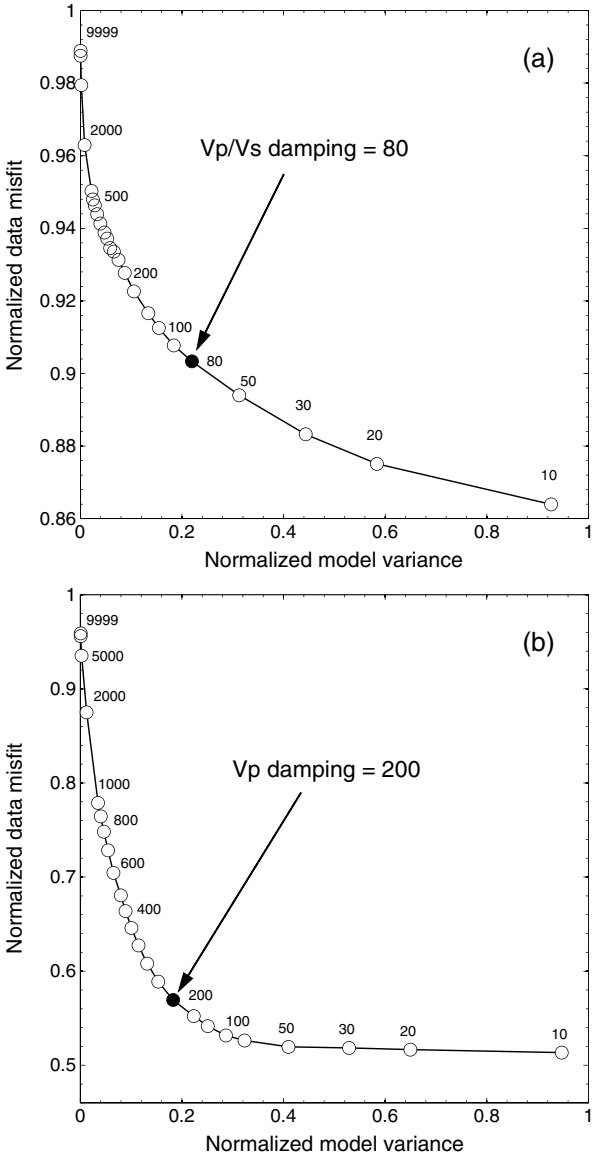

Figure 4. Trade-off curves between data misfit and model variance for simultaneous inversions. (a) For V_p/V_s model, while damping for V_p is held at 200. (b) For V_p model, while damping for V_p/V_s is held at 80.

5. Model Resolution

To assess the model quality, we performed a checkerboard resolution test similar to that in *Lin et al.* [2010]. We computed synthetic times through the 1-D starting velocity model with $\pm 5\%$ V_p and $\mp 5\%$ V_p/V_s perturbations that alternate at different depths and across two grid nodes. Event hypocenters, station locations, and source-receiver pairs have the same distribution as the real data. We also applied the same inversion parameters, such as the damping parameters, as in the real data inversion. Figures 6 and 7 show comparisons between the true and inverted V_p and V_p/V_s models. The white contours enclose the well-resolved area with the diagonal element of the resolution matrix greater than 0.3 for both the V_p and V_p/V_s models, where 1.0 represents the best resolution and 0.0 not resolved at all. Note that the values of the resolution throughout the grid space could be significantly increased by decreasing the damping parameters, but the velocity results may be less reliable.

Our V_p model is generally well resolved between 3 and 20 km depth (Figure 6b1–b6), although some smearing is seen. The good model resolution at deeper layers is owing to the inclusion of events with large epicentral distances (throughout the entire island) and application of the composite event method. The resolution at 1 km depth is limited due to the lack of seismicity at shallow depths, which can be seen from the cross section along profile 1-1′-1″ in Figure 6d. The V_p/V_s model is not resolved as well as the V_p model due to the smaller number of $S-P$ times used in the inversion. The V_p/V_s model is best resolved in the 6 and 9 km depth layers owing to the abundant seismicity in this depth range. From the cross section in Figure 7d, the V_p/V_s model in Mauna Loa is not resolved as well as in Kilauea and strong smearing is observed below 10 km depth.

6. Earthquake Relocation

The crustal and upper mantle velocity structure in the 3-D model provides improved absolute hypocenter locations by correcting for the biasing effects of large-scale velocity variations. After the 3-D model inversion, we use the resulting velocity model to relocate all the background seismicity between 1992 and 2009 on the Island of Hawaii (i.e., the 53,000 events with phase picks instead of the composite events used in the tomographic inversion). In order to improve relative location accuracy during the 3-D location, we combine 3-D ray tracing with the source-specific station term method, similar to the southern California relocation study by *Lin et al.* [2007a]. During the relocation, we use very large damping parameters for V_p and V_p/V_s so that the velocity model is fixed and only the earthquake locations are allowed to change. The 3-D ray tracing

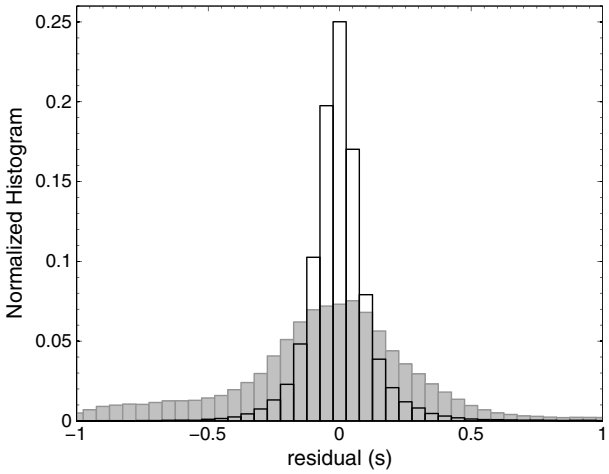

Figure 5. Arrival time residual distributions of the composite events before (gray) and after (black-white) tomographic inversion. The root-mean-square of the residuals drops from 0.40 s to 0.13 s.

and the SSST calculation iterations are repeated 6 times. The absolute location uncertainties in the horizontal and vertical directions are calculated by the simul2000 algorithm as the largest of the horizontal and vertical projections of the principal standard errors for each single event from the last iteration of our inversion. The median location uncertainties are 80 m and 88 m for horizontal and vertical, respectively. Note that our catalog consists of only 40% of the events in the entire HVO catalog that are larger than magnitude 1.0 and have many clear phase picks. The resulting catalog represents a subset of the HVO events with the best location quality.

We then apply the waveform cross correlation, similar event cluster analysis, and differential time location methods described in *Lin et al.* [2007a] to the 3-D relocated events. Cross-correlation information is saved for over 25 million event pairs with an average waveform correlation coefficient of 0.45

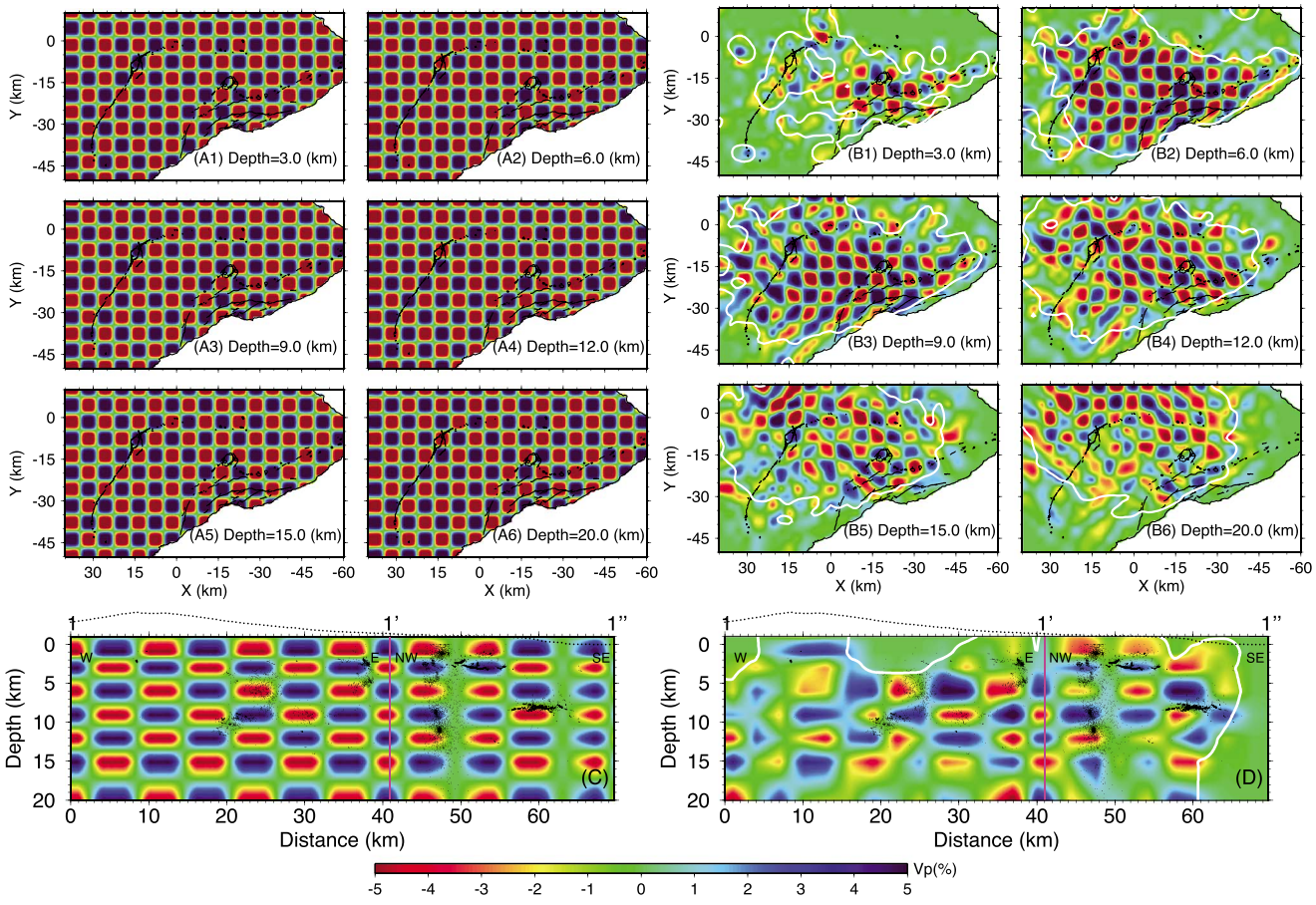

Figure 6. Checkerboard resolution test for the V_p model, in which the synthetic times are computed for the 1-D starting velocity model with ±5% velocity anomalies across two grid nodes. (a1–a6) Map views of the true model. (b1–b6) Map views of the inverted model. (c) Cross section of the true model along profile 1-1′-1″ shown in Figure 3. (d) Cross section of the inverted model along the same profile. The white contours in both map views and cross sections enclose the well-resolved area with the diagonal element of the resolution matrix greater than 0.3. Dotted curves at top of cross sections illustrate the local topography.

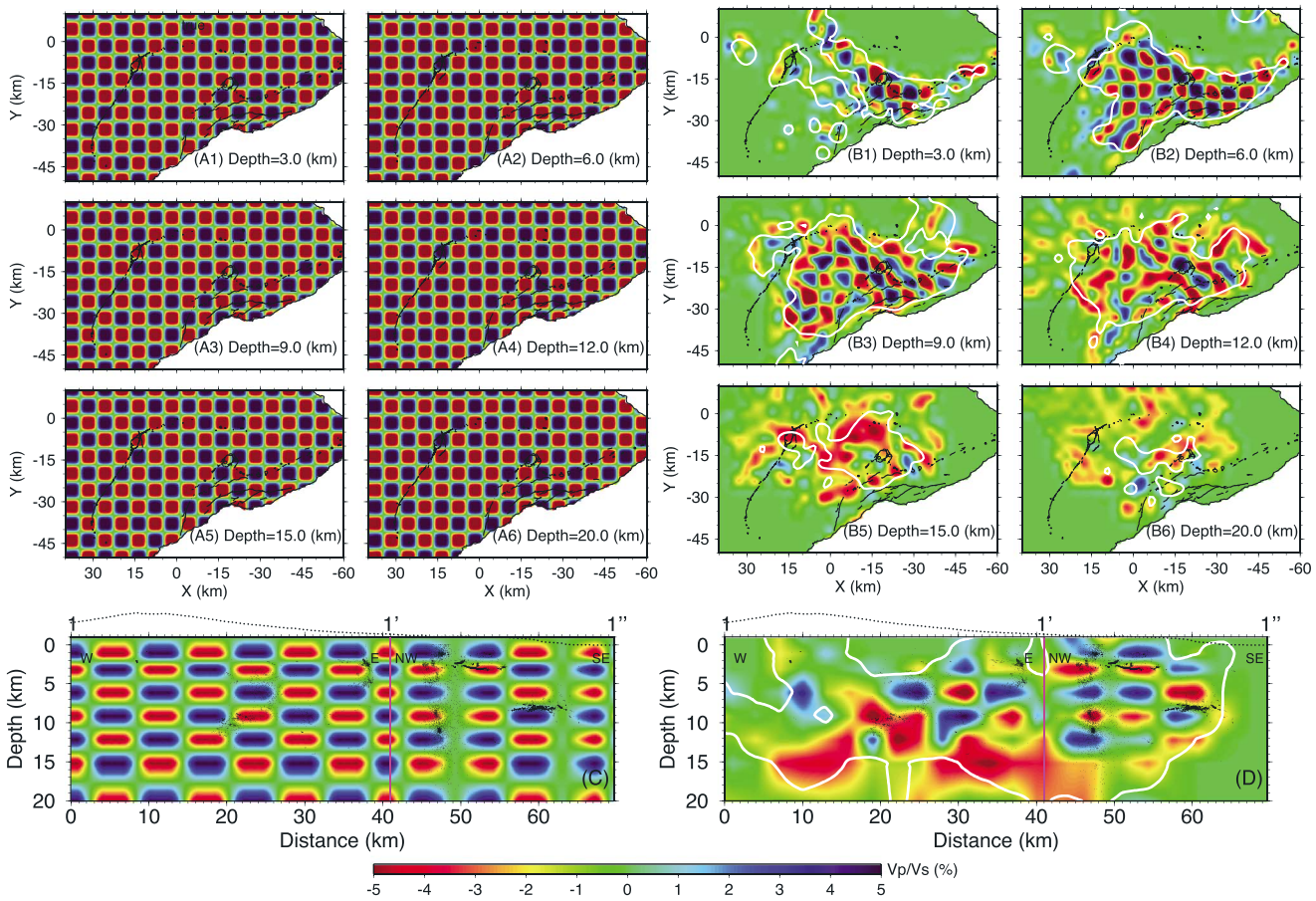

Figure 7. Checkerboard resolution test for the V_p/V_s model, in which the synthetic times are computed for the starting V_p/V_s value with ±5% anomalies across two grid nodes. (a1–a6) Map views of the true model. (b1–b6) Map views of the inverted model. (c) Cross section of the true model along profile 1-1′-1″ shown in Figure 3. (d) Cross section of the inverted model along the same profile. The white contours in both map views and cross sections enclose the well-resolved area with the diagonal element of the resolution matrix greater than 0.3. Dotted curves at top of cross sections illustrate the local topography.

or greater and with at least eight individual differential times with correlation coefficients of 0.6 or greater. Similar parameters were applied to develop a relocation catalog based on a 1-D velocity model for Hawaii by *Matoza et al.* [2013]. Given these criteria, over 56% of all events fall within 337 similar event clusters. The differential time relocation method improves the relative event locations within each cluster using differential times from waveform cross correlation. This method solves for the location of each event directly from all the differential times between each target event and the linked events in the cluster. In order to estimate relative earthquake location uncertainties, we apply a bootstrap approach [*Efron and Gong*, 1983; *Efron and Tibshirani*, 1991], in which the differential times for each event are randomly resampled. This process is repeated 20 times for each event, and we relocate each event using the resampled differential times. We estimate the standard deviations of these 20 subsamples as the standard errors of the relative locations for each event. The median is 18 m for the relative horizontal location uncertainty and 23 m for the vertical location uncertainty.

In Figure 8, we compare the HVO catalog, the 3-D locations, and the waveform cross-correlation relocations along profile 1-1′-1″ (shown in Figure 3). This depth profile passes through some major geological features in our study area, including Mauna Loa caldera, the Kaoiki seismic zone, Kilauea caldera, and the Koae and Hilina fault systems. A slight sharpening of seismicity is observed after the 3-D relocation, but the most significant difference between the HVO and the 3-D catalogs is in absolute location. The 3-D relocated seismicity is about 1 km shallower than the starting locations. A dramatic sharpening of seismicity is obtained by using waveform cross-correlation data. Along this profile, about 53% of the 3-D relocated events fall within similar event clusters. Seismicity in Mauna Loa is more sparse than in Kilauea, and there are only a

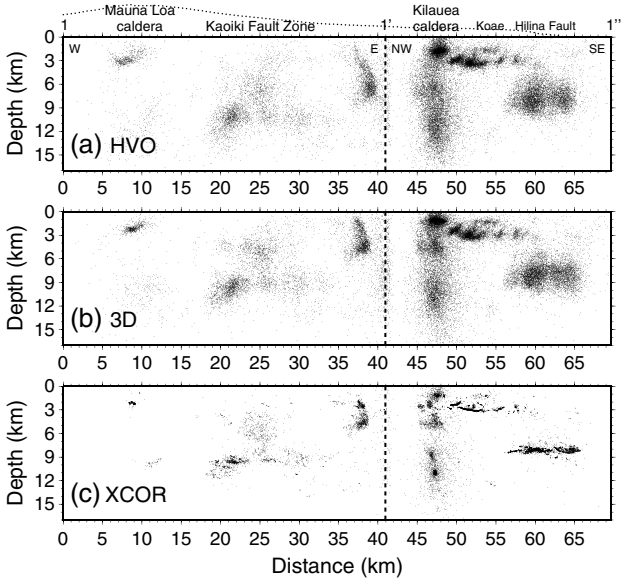

Figure 8. Earthquake locations within ±5 km distance of the profile line 1-1′-1″ (shown in Figure 3) through Mauna Loa caldera, the Kaoiki seismic zone, Kilauea caldera, and the Koae and Hilina fault systems. (a) HVO catalog locations, (b) 3-D relocations, and (c) waveform cross-correlation locations. Great sharpening of seismicity is observed after the differential time relocation. Dotted curves at top illustrate the local topography. Note that along this profile, about 53% of the 3-D relocated events fall within similar event clusters and therefore have differential time relocations.

few event clusters relocated by waveform cross-correlation data beneath the summit. Deep long-period earthquakes have been identified at Mauna Loa [e.g., *Okubo and Wolfe*, 2008] but are not studied in this paper. The Kaoiki seismic zone, where large earthquakes and recurring events have caused damage to buildings and water tanks and triggered numerous landslides, is located approximately halfway between the summit calderas of Mauna Loa and Kilauea. Subhorizontal seismicity planes are relocated between 9 and 12 km depth [*Got et al.*, 1994; *Got and Okubo*, 2003]. Seismicity at Kilauea contains both volcanotectonic and long-period events beneath the summit, with a relatively aseismic zone between 5 and 8 km depth [*Klein et al.*, 1987]. Summit seismicity joins a subhorizontal band in the upper east rift zone at 1–3 km depth [*Gillard et al.*, 1996]. Seismicity associated with a subhorizontal decollement is relocated to 8 km depth (x = 57–66 km, the x axis distance in Figure 8) and agrees with the recent study by *Syracuse et al.* [2010]. A more complete analysis of the relocated 101,390 events based on a 1-D velocity model, including those without phase picks, is presented in *Matoza et al.* [2013].

7. Velocity Model Map Views

7.1. V_p Model

We present our 3-D velocity model in both map views and cross sections. Figure 9 shows map-view slices of the *P* velocity perturbations relative to the layer-average values at each layer between 3 and 20 km depth. The white contours enclose the well-resolved areas with the diagonal element of the resolution matrix greater than 0.3. Due to the sparse seismicity near the surface, the model resolution is limited at 1 km depth, and we do not show it here. The model is well resolved between 3 and 20 km depth.

The most notable features in the V_p model are the high-velocity anomalies near Mauna Loa and Kilauea calderas and their rift zones within the first two depth layers. At 3 km depth, the highest velocity of above 6.8 km/s occurs near Mauna Loa caldera and its southwest rift zone and is about 15–28% (6.0–6.6 km/s) higher than the layer-average value (5.21 km/s). The model also shows high-velocity anomalies of up to 21% (6.3 km/s) relative to the layer-average value near the Kilauea caldera and its rift zones. A small low-velocity body is visible near Halema'uma'u crater. The Kaoiki seismic zone and Hilina fault system both show low-velocity anomalies and the perturbations relative to the 1-D layer-average model are about 18% (4.2 km/s) near the Hilina fault system. A similar velocity anomaly pattern is seen at 6 km depth, where the model resolution is much better than in the upper layer. The velocity anomaly near Mauna Loa caldera is slightly reduced to about 12% (7.5 km/s) higher than the layer-average value (6.69 km/s). Clearly seen in this layer are (spanning from the west to the east side of the study area) the high-velocity anomalies for Mauna Loa and its rift zones, low-velocity anomalies in the Kaoiki seismic zone, high-velocity anomalies at Kilauea and its rift zones, and low-velocity anomalies near the Hilina fault system. At 9 km depth, the model starts to show low-velocity bodies along the rift zones of both Mauna Loa and Kilauea. The highest velocity still occurs near Mauna Loa caldera. The two layers at 6 and 9 km depth are the best-resolved layers in our model owing to the abundant seismicity in this depth range. Similar features are seen at 12 km depth, but

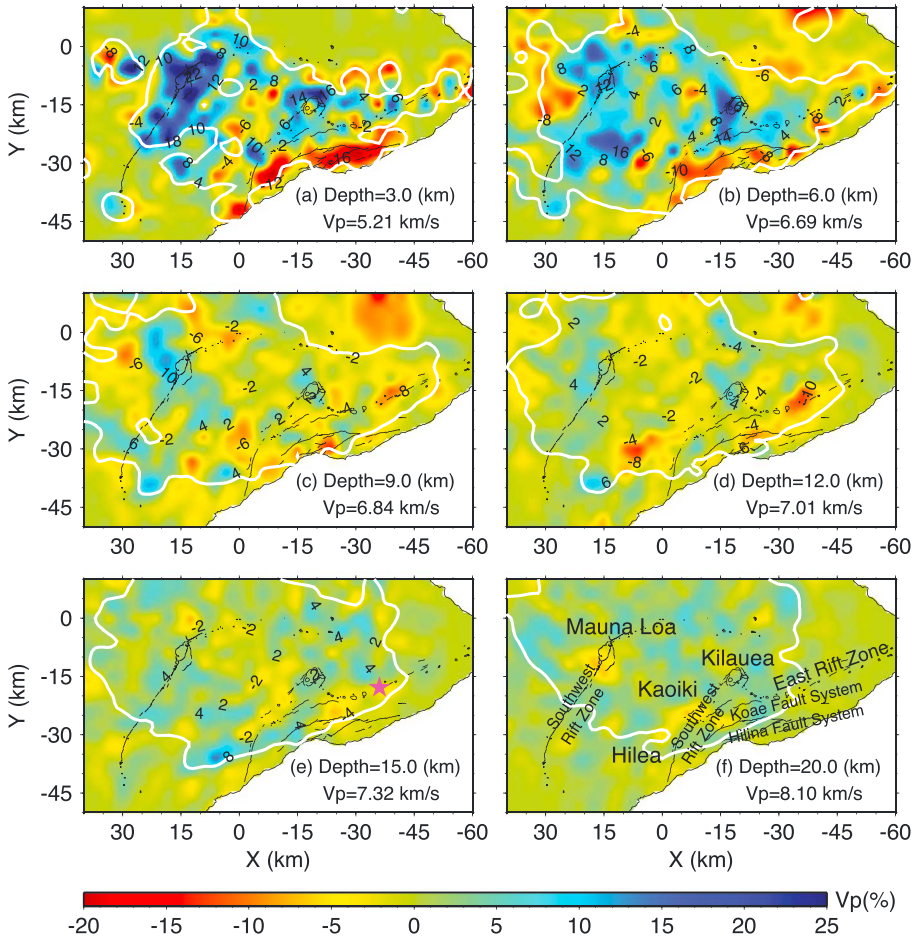

Figure 9. (a–f) Map views of the *P* wave velocity perturbations relative to the layer-average values at each depth slice. Black lines denote the coast line and surface traces of mapped faults. The white contours enclose the well-resolved area with the diagonal element of the resolution matrix greater than 0.3. The average velocity value is also shown for each depth. Major geological features in this area are Mauna Loa caldera and its rift zones, Kilauea and its rift zones, the Kaoiki and Hilea seismic zones between the two calderas, and the Koae and Hilina fault systems. Pink star in Figure 9e is the location of Pu'u 'O'o, where a long-term eruption started in 1983.

the velocity contrasts become weaker. The V_p model is relatively uniform at 15 and 20 km depth with only a few percent velocity variations.

7.2. V_p/V_s Model

The great number of *S* wave arrivals from the composite events enables the development of a V_p/V_s model with fairly good resolution in our study area. Figure 10 shows map view slices of the V_p/V_s model at different depths between 3 and 20 km. White contours enclose the reasonably well-resolved area with the diagonal element of the resolution matrix greater than 0.3. At 3 km depth, the well-resolved area is dominated by relatively low-V_p/V_s ratios (below 1.65). A few high-V_p/V_s bodies are seen near Kilauea caldera and its upper and lower east rift zones. In contrast to the low-V_p/V_s anomalies in this layer, the next two layers are dominated by high-V_p/V_s ratios (above 1.8) and are again the best-resolved layers in our model. At 6 km depth, the lowest values of approximately 1.6 occur near the Hilea seismic zone and the Koea fault system. High-V_p/V_s ratios of above 1.85 are observed in the areas surrounding the two calderas. However, the calderas themselves show somewhat low-V_p/V_s ratios, especially in Mauna Loa, where a relatively low-V_p/V_s body is visible. This feature changes at 9 km depth where low-V_p/V_s ratios are shown in the vicinity of Kilauea caldera, but high-V_p/V_s values are prominent near Mauna Loa. The Kaoiki seismic zone between the two calderas is dominated by high-V_p/V_s anomalies, whereas the Hilea seismic zone, the Hilina fault system, and the lower east rift zone of Kilauea show low-V_p/V_s ratios. Similar patterns are observed at 12 km depth,

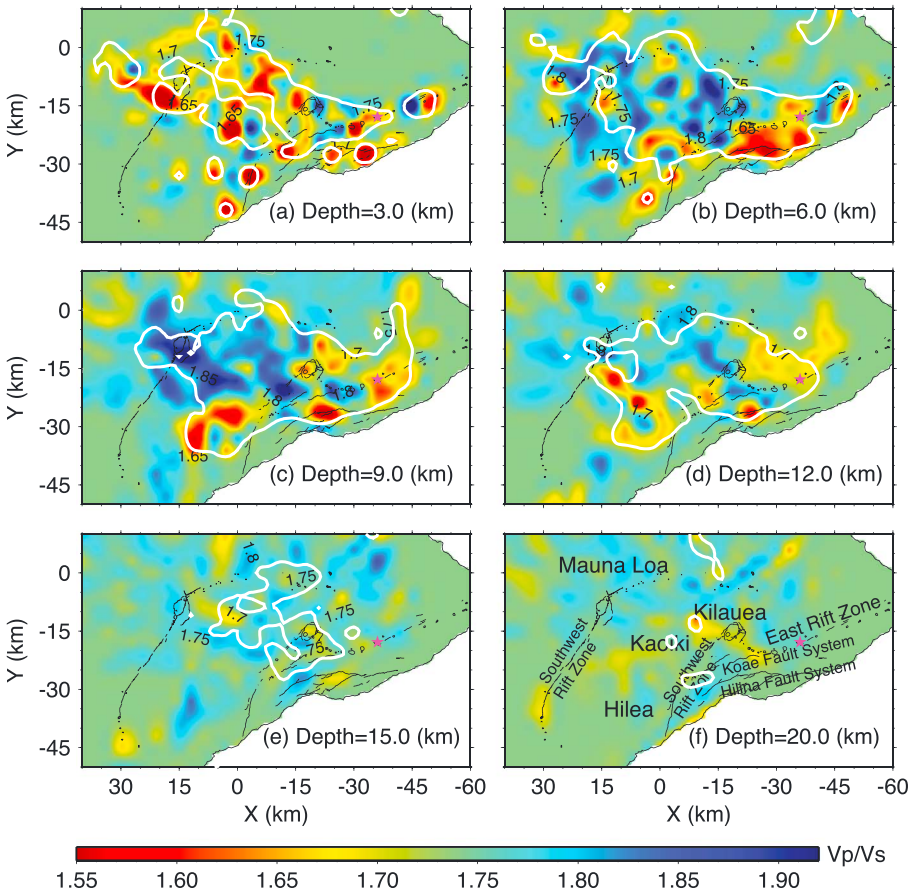

Figure 10. Map views of the V_p/V_s model at different depth slices. Black lines denote the coast line and surface traces of mapped faults. The white contours enclose the well-resolved area with the diagonal element of the resolution matrix greater than 0.3. The major geological features are the same as in Figure 9.

but the V_p/V_s contrasts are significantly reduced. The V_p/V_s ratios in the last two layers are relatively uniform with very limited resolution, varying between 1.7 and 1.8.

8. Cross Sections

Cross sections of our V_p and V_p/V_s models are shown in Figures 11 and 12. Note that the black dots in these figures are the background seismicity relocated by using waveform cross-correlation data, instead of the composite events used in the tomographic inversions.

8.1. Mauna Loa Volcano

In Figure 11, cross sections are shown along two profiles near Mauna Loa. Profile A-A′ runs along the southwest rift zone of Mauna Loa (shown in Figures 11a and 11b). A high-velocity body of 7.5 km/s is observed between 5 and 10 km depth beneath the caldera, which may represent the mafic magmatic cumulates that form the core of the caldera and rift zones of Mauna Loa [*Hill and Zucca*, 1987; *Okubo et al.*, 1997]. The southwest flank also shows high-velocity anomalies from 0 to 6 km depth compared to Kilauea's flank, although slightly weaker than its own caldera area. The V_p/V_s model along the same profile is only resolved near the caldera. As shown in the map views, the V_p/V_s ratios are quite low from 0 to 6 km depth but become very high between 6 and 15 km depth. The seismicity is rather sparse in this area. Only two small event clusters are relocated at 2 km depth at the edge of a very low-V_p/V_s body. A low-V_p body imaged with limited resolution is centered at 9 km depth (x = 20–28 km), which could be an indication of partial melt. However, the unresolved V_p/V_s model in this area cannot put additional constraints on this.

Profile B-B′ cuts across the southeast flank of Mauna Loa starting from the caldera through the Kaoiki and Hilea seismic zones to the coast. The most striking feature along this profile is the velocity contrast between

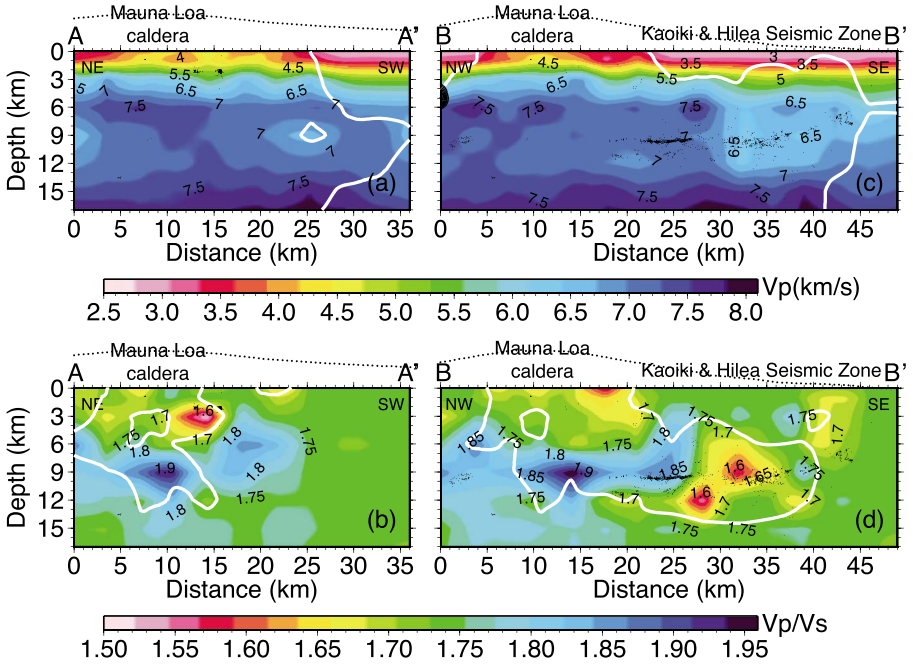

Figure 11. Cross sections through our V_p and V_p/V_s model along two profiles across Mauna Loa caldera (A-A' and B-B' in Figure 3). Black dots represent the cross-correlation relocated background seismicity within ±3 km distance of the profile line. The white contours enclose the well-resolved area with the diagonal element of the resolution matrix greater than 0.3. Dotted curves at top illustrate the local topography.

the seismic zone and the summit caldera along with its southeast flank. The velocity near the caldera is higher than the adjacent area throughout the entire depth range. The shallow velocity is up to 40% higher than the nearby regions. The velocity between 6 and 13 km depth is reduced from 7.5 km/s beneath the caldera to 7 km/s in the southeast flank and then 6.5 km/s beneath the Hilea seismic zone. The low-velocity regions in the active fault systems are observed in previous studies extending to 6–8 km depth [e.g., *Okubo et al.*, 1997], but the velocity contrast with the high-velocity anomalies to the NW side are visible down to 13 km depth in this study. Corresponding to the low-V_p bodies, low-V_p/V_s ratios are observed in the middle crust of the seismic zones, which may be due to water-filled pores with high aspect ratios [e.g., *Lin and Shearer*, 2009]. The seismicity is relocated as subhorizontal linear features within this low-V_p/V_s body, which contrasts strongly with the high values of ~1.80 in the summit area. Similar to A-A', low-V_p/V_s ratios are shown near Mauna Loa caldera and its southeast flank from 0 to 6 km depth. Below 6 km depth, very high-V_p/V_s anomalies are observed in the depth range of 7–17 km. Part of the relocated seismicity is distributed within this high-V_p/V_s body. The majority of the seismicity along this profile is distributed between 7 and 11 km depth.

8.2. Kilauea Volcano

Kilauea is much more extensively studied than Mauna Loa owing to its abundant seismicity. In Figures 12a and 12b, we show velocity variations along the southwest rift zone of Kilauea. The most striking features along this profile are the high-velocity anomalies and great seismic activity beneath the caldera. The *P* wave velocity below the summit is slightly higher than the proximate area near the surface, which can be seen from a close-up of the shallow-V_p structure in Figure 12e. Low-velocity anomalies are visible between 1.6 and 3.6 km depth (see Figure 12e), which was also observed in some previous studies with a slightly different depth range [e.g., *Thurber*, 1984, 1987; *Rowan and Clayton*, 1993; *Dawson et al.*, 1999] and was interpreted as the seismic expression of the summit magma reservoir. Right below this, a high-V_p body of ~7.5 km/s is situated between 5 and 8 km depth. The velocities below the high-velocity body are slightly lower than 7.5 km/s, but still higher than in other regions along this profile at the same depth. On the southwest side of the caldera, relatively low velocities are observed throughout the entire flank, especially below 6 km depth. The most extreme anomalies between x = 26 and 38 km start at 5 km depth and stop at about 12 km depth near the Kaoiki and Hilea seismic zone, similar to the anomalies seen in Figure 11c.

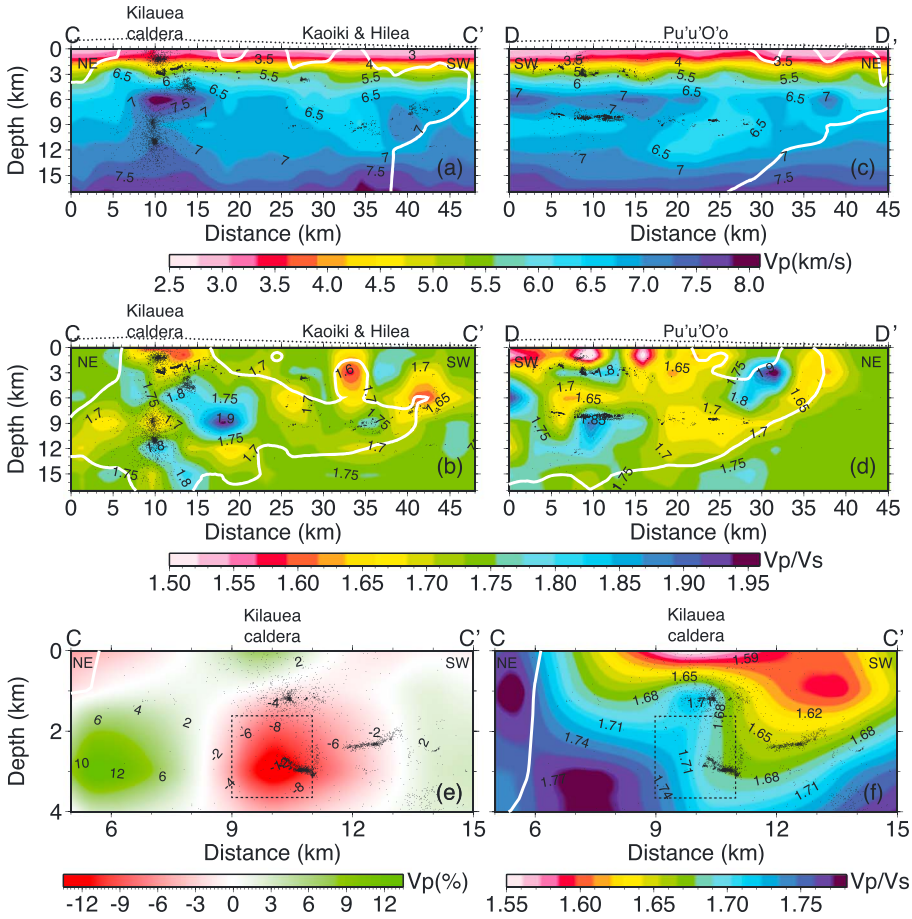

Figure 12. (a–f) Cross sections through our V_p and V_p/V_s model along two profiles across Kilauea caldera (C-C′ and D-D′ in Figure 3). Black dots represent the cross-correlation relocated background seismicity within ±3 km distance of the profile line. The white contours enclose the well-resolved area with the diagonal element of the resolution matrix greater than 0.3. Dotted curves at top illustrate the local topography. Figures 12e and 12f show close-up views of the shallow structure near the summit along profile C-C′. For the V_p model in Figure 12e, perturbations relative to depth-average at 0.5 km interval are shown.

Immediately adjacent on the southwest side, another high-velocity body is seen between 6 and 13 km depth. The seismicity in this cross section is mainly focused near Kilauea caldera. Several event clusters are relocated in the summit area (x = 7–15 km), with one centered at about 1 km depth and another one at 3 km depth (also in Figure 12e). The seismicity becomes sparse below 4 km depth, and this aseismic zone coincides with the high-V_p body. Active seismicity continues at 8 km depth right below the high-velocity body. The V_p/V_s model in Kilauea is much more anomalous than for Mauna Loa. The most significant variations occur below Kilauea caldera. The V_p/V_s model at shallow depths is dominated by low values (<1.7). The V_p/V_s ratios corresponding to the low-V_p anomalies between 1.6 and 3.6 km depth do not show significant high-V_p/V_s anomalies but vary between 1.68 and 1.74 (see a close-up of the shallow V_p/V_s structure in Figure 12f), which is inconsistent with the existence of shallow magma. A high-V_p/V_s body cuts across between 4 and 7 km depth, which continues to the highest-V_p/V_s body along this profile between 6 and 11 km depth (x = 12–22 km) on the southwest side. A very low-V_p/V_s body is centered at 9 km depth below the summit and is followed by a high-V_p/V_s body at 12 km depth. The southwest rift zone of Kilauea is generally dominated by low-V_p/V_s anomalies.

Velocity variations in the East Rift Zone (ERZ) of Kilauea are shown along profile D-D′ (Figures 12c and 12d). Both the V_p and V_p/V_s models in the upper ERZ are more anomalous than in the middle and lower east rift zones. The upper ERZ is dominated by high-V_p values (>7.0 km/s) from 5 to 8 km depth. Below this, low-V_p structure is visible between 8 and 11 km depth. The seismicity along this profile is mainly focused in this area and occurs at the boundary of the high- and low-velocity bodies. The most striking feature beneath

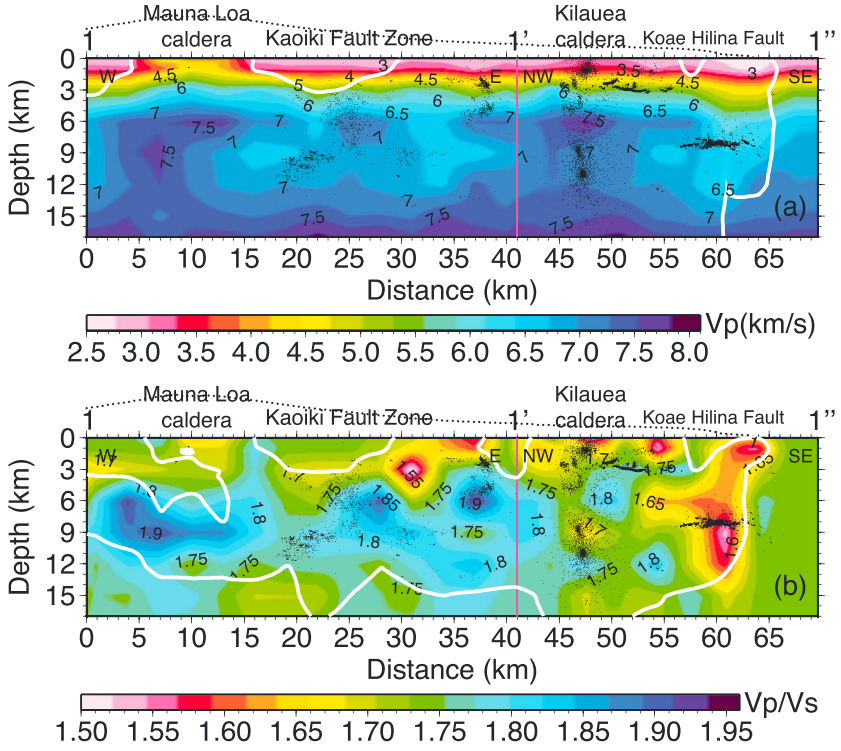

Figure 13. Cross sections through our V_p and V_p/V_s model along two connected profiles (1-1′ and 1′-1″ in Figure 3) across some major geological features in the study area, including Mauna Loa caldera, the Kaoiki seismic zone, Kilauea caldera, and the Koae-Hilina fault system. Black dots represent the cross-correlation relocated background seismicity within ±3 km distance of the profile line. The white contours enclose the well-resolved area with the diagonal element of the resolution matrix greater than 0.3. Dotted curves at top illustrate the local topography.

the middle ERZ is the low-velocity body (x∼15–33 km) from 5 to 14 km depth. Pu'u 'O'o-Kupaianaha (a vent 3 km down rift) is located at x = 22 km, where there has been a long-lived eruption since 1983. The model resolution in the lower ERZ is limited at deeper layers, but the model shows great variations shallower than 9 km depth. Along this profile, the V_p/V_s model shows complex low- and high-anomaly patterns, especially in the upper ERZ. The V_p/V_s ratio corresponding to the high-V_p structure between 5 and 8 km depth is less than 1.7. Below it a high-V_p/V_s body is observed where the low-V_p body exists. The middle ERZ is dominated by low-V_p/V_s ratios (<1.7) from 0 to 15 km depth. *Poland et al.* [2013] suggested that the increased supply at Pu'u 'O'o-Kupaianaha during 2003–2007 must have been driven by increased flux of magma from the mantle, which is supported by increased CO_2 emissions. The low-V_p and low-V_p/V_s anomalies observed in our model are consistent with the existence of CO_2 and were also observed by *Hansen et al.* [2004]. The resolved area in the lower ERZ has one high- and one low-V_p/V_s body next to each other.

9. Discussion

In Figure 13, we present the velocity variations along profile 1-1′-1″ across Mauna Loa caldera, the Kaoiki seismic zone, Kilauea caldera and its upper east rift zone, and the Hilina fault zone. The most notable features of our V_p model along this profile are the velocity contrasts between the fault systems and the two calderas along with their rift zones. The V_p/V_s model shows more complex variation patterns with relatively limited resolution. The velocity structures along this profile clearly show the difference between Mauna Loa and Kilauea volcanoes. Beneath the Mauna Loa caldera, we observe high-V_p (∼7–7.5 km/s) and high-V_p/V_s (1.8–1.9) values between 5 and 12 km depth. The high-V_p anomalies are often interpreted as mafic/ultramafic magmatic cumulates [*Hill and Zucca*, 1987; *Okubo et al.*, 1997], which usually have high-V_p/V_s ratios because they contain gabbro and peridotite originating from magmatic differentiation [*Christensen*, 1996]. At about the same depth range in the Kaoiki seismic zone, high-V_p/V_s ratios (1.8–1.85) are also observed, but the corresponding V_p model shows relatively low velocities of about 6–7 km/s, which

may have a similar origin as that of the Hilina fault zone and can be attributed to preexisting volcaniclastic submarine sediments [*Park et al.*, 2007].

The area beneath the Kilauea caldera and its upper ERZ is generally dominated by high-V_p anomalies with a complex V_p/V_s pattern. One striking feature is the high-V_p body (7–7.5 km/s) beneath the summit below 5 km depth with moderate to relatively low-V_p/V_s ratios between 1.7 and 1.8. As indicated by the petrologic model of *Shillington et al.* [2013] for a different tectonic setting, high-V_p and low-V_p/V_s features can be best explained by a combination of mafic compositions rather than single composition models. A decrease of V_p/V_s ratio can be caused by changing from gabbro to olivine-rich gabbro and dunite due to the decreasing amounts of plagioclase feldspar and increasing olivine content [*Christensen*, 1996]. In the southeast flank of Kilauea, low-V_p (<6.5 km/s) and V_p/V_s (<1.65) anomalies are prominent from 0 to 15 km depth. *Hansen et al.* [2004] attributed an anomalous body of low V_p and low V_p/V_s at 7 km depth in the ERZ to a trapped CO_2 reservoir. The difference in our study is the large depth range that this anomaly spans. In order to reduce the V_p/V_s ratio to such a low level (<1.65), the presence of quartz is usually expected [*Christensen*, 1996]. However, no observations of quartz over such a large spatial scale have been seen in this area. Another possible explanation for the reduced V_p and V_p/V_s is the presence of fluid. A recent study in southern California by *Lin and Shearer* [2009] identified a correlation between seismic activity and low-V_p/V_s ratios within similar event clusters and argued that this suggested water-filled cracks in earthquake source regions. *Lin* [2013] observed low-V_p/V_s ratios in a near-vertical zone at shallow depths beneath Mammoth Mountain, California, suggesting involvement of fluid in the upward migration of the seismicity. Here we attribute the low V_p and V_p/V_s in the Hilina Fault System to the volatile content of the magma from the mantle and the active fault zones provide paths for its escape to the surface.

9.1. Comparison With Previous Studies

The *P* velocity structure in Hawaii, especially near Kilauea volcano, has been investigated by a great number of studies. One of the main differences between this study and previous ones is the improved V_p model resolution at deeper layers owing to the inclusion of events with large epicentral distances and application of the composite event method. Our V_p model is well resolved to 20 km depth near the volcano calderas and their rift zones (Figure 6) and generally agrees with the previous models [*Ryall and Bennett*, 1968; *Hill*, 1969; *Ellsworth and Koyanagi*, 1977; *Zucca and Hill*, 1980; *Thurber*, 1984; *Rowan and Clayton*, 1993; *Okubo et al.*, 1997; *Dawson et al.*, 1999; *Haslinger et al.*, 2001; *Hansen et al.*, 2004; *Monteiller et al.*, 2005; *Park et al.*, 2007; *Got et al.*, 2008; *Park et al.*, 2009; *Syracuse et al.*, 2010]. The common features observed in these studies and also in our model are the high-velocity anomalies in the upper 9 km depth beneath Kilauea caldera and its rift zones, indicative of magma cumulates. In contrast to these high velocities, the low-velocity perturbations in the Kaoiki seismic zone are attributed to thick piles of volcaniclastic sediments deposited on the submarine flanks [*Park et al.*, 2007], whereas the velocity anomalies in the southeast flank of Kilauea (near the Hilina fault system) may be explained by the presence of hyaloclastites and volcaniclastic sediments [*Park et al.*, 2007; *Syracuse et al.*, 2010]. Below Kilauea caldera, we observe a low-V_p body coinciding with an aseismic zone between 1.6 and 3.6 km depth, which was also observed in some of the previous studies [e.g., *Thurber*, 1984, 1987; *Rowan and Clayton*, 1993; *Dawson et al.*, 1999] and was interpreted as the seismic expression of the summit magma reservoir. The *P* velocity structure for the Mauna Loa area was obtained in several previous studies [e.g., *Okubo et al.*, 1997; *Monteiller et al.*, 2005; *Park et al.*, 2007, 2009]. A striking feature in our V_p model is the remarkably high-velocity anomalies beneath Mauna Loa caldera throughout the entire depth range. *Park et al.* [2007] interpreted the high-velocity anomalies along the southeast flank as an inactive buried volcanic rift zone.

V_p/V_s models help constrain the composition of rocks, the presence of cracks, the degree of pore fluid saturation, and other properties. Although the resolution of the V_p/V_s model is not as good as the V_p model, the model is relatively well resolved near the two calderas to 12 km depth (Figure 7). Our V_p/V_s model shows large variations from 0 to 20 km depth and is dominated by lower values at shallow depths. Near Mauna Loa caldera, the V_p/V_s model can be summarized as having low values near the surface and high-ratio anomalies between 5 and 15 km depth, although the model resolution is quite poor. The structure is more complicated beneath Kilauea caldera, as both low- and high-V_p/V_s values are observed all the way to 20 km depth. In contrast to the large variations at the calderas and rift zones, the Hilina fault zone shows systematically low-V_p/V_s ratios. Compared with studies on the V_p structure, relatively few V_p/V_s models are available. *Dawson et al.* [1999] observed a low-velocity *P* wave anomaly and corresponding high-V_p/V_s body from 1 km above to 2.5 km below sea level centered on the southeastern edge of the caldera, which was

interpreted as a densely cracked body containing partial melt. We also observe a low-*P* velocity body between 1.6 and 3.6 km depth. However, the V_p/V_s ratio in this area is lower than the starting value of 1.74, although higher than ratios in the surrounding regions (Figures 12e and 12f). This observation is more consistent with the presence of gas instead of partial melt. *Johnson and Poland* [2013] proposed that increased degassing can explain a decrease in V_p/V_s ratios and variations in shear wave splitting before Kilauea's 2008 summit explosion. *Hansen et al.* [2004] resolved V_p, V_p/V_s, and attenuation models in the ERZ of Kilauea by inverting seismic data recorded by temporary and HVO stations. They observe a low-velocity zone beneath and south of the Hilina Pali. Differing from their result, systematically low-V_p/V_s ratios from the surface to 15 km depth are observed in this study. An anomalous body with low-V_p, low-V_s, and high-V_p/V_s value is resolved at 8–11 km depth beneath the upper ERZ of Kilauea volcano. *Lin et al.* [2014] recently suggested the presence of 10% melt in a cumulate magma mush in this area based on petrophysical modeling.

10. Conclusions

In this paper, we present a new 3-D seismic velocity model for the crustal and upper mantle structure of Mauna Loa and Kilauea volcanoes in Hawaii. Our *P* velocity model generally agrees with previous studies, showing high-velocity anomalies at depth below the calderas and rift zones and low-velocity anomalies in the fault systems. The V_p/V_s model is a major result of this study, owing to the application of the composite event method. In the vicinity of Mauna Loa volcano, the V_p/V_s model is dominated by relatively low values near the surface and high ratios between 5 and 15 km depth. The V_p/V_s model shows large variations beneath the Kilauea summit. Systematically, low-V_p/V_s ratios are observed in the southeast flank of Kilauea. A by-product of this study is an improved earthquake location catalog by combining 3-D ray tracing and differential time relocation methods. The improvement in relative location accuracy obtained by using waveform cross-correlation data produces a dramatic sharpening of the seismicity patterns. The 3-D velocity model and earthquake relocation catalog are available as supplemental material and also at http://www.rsmas.miami.edu/users/glin/Hawaii.html.

Acknowledgments

We thank the USGS Hawaiian Volcano Observatory for maintaining the seismic network and making the data available. We are grateful to Jeanne Hardebeck and two anonymous reviewers for their constructive and detailed comments. Plots were made using the public domain GMT software and MATLAB. Data for this paper are available in the supporting information. Funding for this research was provided by the National Science Foundation grant EAR-1246935.

References

Amelung, F., S.-H. Yun, T. R. Walter, P. Segall, and S.-W. Kim (2007), Stress control of deep rift intrusion at Mauna Loa volcano, Hawaii, *Science*, *316*, 1026–1030.

Brooks, B. A., J. Foster, D. Sandwell, C. J. Wolfe, P. Okubo, M. Poland, and D. Myer (2008), Magmatically triggered slow slip at Kilauea volcano, Hawaii, *Science*, *321*, 1177.

Cayol, V., J. Dieterich, A. Okamura, and A. Miklius (2000), High magma storage rates before the 1983 eruption of Kilauea, Hawaii, *Science*, *288*, 2343–2346.

Christensen, N. I. (1996), Poisson's ratio and crustal seismology, *J. Geophys. Res.*, *101*, 3139–3156.

Dawson, P. B., B. Chouet, J. C. Lahr, and R. A. Page (1992), Spatial relationship between LP earthquakes and a shallow three-dimensional velocity anomaly beneath Redoubt Volcano, Alaska, *Eos, Trans. AGU*, *73*, 343.

Dawson, P. B., B. A. Chouet, P. G. Okubo, A. Villaseñor, and H. M. Benz (1999), Three-dimensional velocity structure of the Kilauea Caldera, Hawaii, *Geophys. Res. Lett.*, *26*, 2805–2808.

Dziewonski, A. M. (1984), Mapping the lower mantle: Determination of lateral heterogeneity in P velocity up to degree and order 6, *J. Geophys. Res.*, *89*, 5929–5952.

Eberhart-Phillips, D. (1986), Three-dimensional velocity structure in the northern California Coast Ranges from inversion of local earthquake arrival times, *Bull. Seismol. Soc. Am.*, *76*, 1025–1052.

Eberhart-Phillips, D. (1990), Three-dimensional P and S velocity structure in the Coalinga region, California, *J. Geophys. Res.*, *95*, 15,343–15,363.

Eberhart-Phillips, D. (1993), Local earthquake tomography: Earthquake source regions, in *Seismic Tomography: Theory and Practice*, edited by H. M. Iyer and K. Hirahara, pp. 613–643, Chapman and Hall, London, U. K.

Efron, B., and G. Gong (1983), A leisurely look at the bootstrap, the jackknife and cross-validation, *Am. Stat.*, *37*, 36–48.

Efron, B., and R. Tibshirani (1991), Statistical data analysis in the computer age, *Science*, *253*, 390–395.

Ellsworth, W., and R. Koyanagi (1977), Three-dimensional crust and mantle structure of Kilauea Volcano, Hawaii, *J. Geophys. Res.*, *82*, 5379–5394.

Evans, J. R., D. Eberhart-Phillips, and C. H. Thurber (1994), User's manual for SIMULPS12 for imaging Vp and Vp/Vs: A derivative of the "Thurber" tomographic inversion SIMUL3 for local earthquakes and explosion, *U.S. Geol. Surv. Open File Rep.*, *94-431*.

Gillard, D., A. M. Rubin, and P. Okubo (1996), Highly concentrated seismicity caused by deformation of Kilauea's deep magma system, *Nature*, *384*, 343–346.

Got, J.-L., and P. Okubo (2003), New insights into Kilauea's volcano dynamics brought by large-scale relative relocation of microearthquakes, *J. Geophys. Res.*, *108*(B7), 2337, doi:10.1029/2002JB002060.

Got, J.-L., J. Fréchet, and F. W. Klein (1994), Deep fault plane geometry inferred from multiplet relative relocation beneath the south flank of Kilauea, *J. Geophys. Res.*, *99*, 15,375–15,386.

Got, J.-L., V. Monteiller, J. Monteux, R. Hassani, and P. Okubo (2008), Deformation and rupture of the oceanic crust may control growth of Hawaiian volcanoes, *Nature*, *451*, 453–456.

Hansen, S., C. Thurber, M. Mandernach, F. Haslinger, and C. Doran (2004), Seismic velocity and attenuation structure of the east rift zone and south flank of Kilauea volcano, Hawaii, *Bull. Seismol. Soc. Am.*, *94*, 1430–1440.

Haslinger, F., C. Thurber, M. Mandernach, and P. Okubo (2001), Tomographic image of P-velocity structure beneath Kilauea's East Rift Zone and South Flank: Seismic evidence for a deep magma body, *Geophys. Res. Lett.*, *28*, 375–378.
Hill, D. P. (1969), Crustal structure of the Island of Hawaii from seismic-refraction measurements, *Bull. Seismol. Soc. Am.*, *59*, 101–130.
Hill, D. P., and J. J. Zucca (1987), Geophysical constraints on the structure of Kilauea and Mauna Loa volcanoes and some implications for seismomagmatic processes, *U.S. Geol. Surv. Prof. Pap.*, *1350*, 903–917.
Hill, D. P., F. Pollitz, and C. Newhall (2002), Earthquake-volcano interactions, *Phys. Today*, *55*, 41–47.
Johnson, J. H., and M. P. Poland (2013), Seismic detection of increased degassing before Kilauea's 2008 summit explosion, *Nat. Commun.*, *4*, 1668.
Klein, F. W. (1981), A linear gradient crustal model for south Hawaii, *Bull. Seismol. Soc. Am.*, *71*, 1503–1510.
Klein, F. W., R. Y. Koyanagi, J. S. Nakata, and W. R. Taxtigawa (1987), The seismicity of Kilauea's magma system, *U.S. Geol. Surv. Prof. Pap.*, *1350*, 1019–1186.
Lin, G. (2013), Seismic investigation of magmatic unrest beneath Mammoth Mountain, California using waveform cross-correlation, *Geology*, *41*, 847–850, doi:10.1130/G34062.1.
Lin, G., and P. M. Shearer (2009), Evidence for water-filled cracks in earthquake source regions, *Geophys. Res. Lett.*, *36*, L17315, doi:10.1029/2009GL039098.
Lin, G., P. M. Shearer, and E. Hauksson (2007a), Applying a three-dimensional velocity model, waveform cross correlation, and cluster analysis to locate southern California seismicity from 1981 to 2005, *J. Geophys. Res.*, *112*, B12309, doi:10.1029/2007JB004986.
Lin, G., P. M. Shearer, E. Hauksson, and C. H. Thurber (2007b), A three-dimensional crustal seismic velocity model for southern California from a composite event method, *J. Geophys. Res.*, *112*, doi:10.1029/2007JB004977.
Lin, G., C. H. Thurber, H. Zhang, E. Hauksson, P. M. Shearer, F. Waldhauser, T. M. Brocher, and J. Hardebeck (2010), A California statewide three-dimensional seismic velocity model from both absolute and differential times, *Bull. Seismol. Soc. Am.*, *100*, 225–240.
Lin, G., F. Amelung, Y. Lavallee, and P. G. Okubo (2014), Seismic evidence for a crustal magma reservoir beneath the upper east rift zone of Kilauea volcano, Hawaii, *Geology*, *42*, 187–190, doi:10.1130/G35001.1.
Lipman, P., J. Lockwood, R. Okamura, D. Swanson, and K. Yamashita (1985), Ground deformation associated with the 1975 magnitude-7.2 earthquake and resulting changes in activity of Kilauea Volcano, Hawaii, *U.S. Geol. Surv. Prof. Pap.*, *1276*.
Matoza, R. S., P. M. Shearer, G. Lin, C. J. Wolfe, and P. G. Okubo (2013), Systematic relocation of seismicity on Hawaii Island from 1992 to 2009 using waveform cross correlation and cluster analysis, *J. Geophys. Res. Solid Earth*, *118*, 2275–2288.
Monteiller, V., J. Got, J. Virieux, and P. Okubo (2005), An efficient algorithm for double-difference tomography and location in heterogeneous media, with an application to the Kilauea volcano, *J. Geophys. Res.*, *110*, B12306, doi:10.1029/2004JB003466.
Okubo, P. G., and C. J. Wolfe (2008), Swarms of similar long-period earthquakes in the mantle beneath Mauna Loa Volcano, *J. Volcanol. Geotherm. Res.*, *178*, 787–794.
Okubo, P. G., H. M. Benz, and B. A. Chouet (1997), Imaging the crustal magma sources beneath Mauna Loa and Kilauea volcanoes, Hawaii, *Geology*, *25*, 867–870.
Park, J., J. K. Morgan, C. A. Zelt, P. G. Okubo, L. Peters, and N. Benesh (2007), Comparative velocity structure of active Hawaiian volcanoes from 3-D onshore-offshore seismic tomography, *Earth Planet. Sci. Lett.*, *259*, 500–516.
Park, J., J. K. Morgan, C. A. Zelt, and P. G. Okubo (2009), Volcano-tectonic implications of 3-D velocity structures derived from joint active and passive source tomography of the island of Hawaii, *J. Geophys. Res.*, *114*, B09301, doi:10.1029/2008JB005929.
Pavlis, G. L., and J. R. Booker (1980), The mixed discrete-continuous inverse problem: application to the simultaneous determination of earthquake hypocenters and velocity structure, *J. Geophys. Res.*, *85*, 4801–4810.
Poland, M. P., A. Miklius, and E. K. Montgomery-Brown (2013), Magma supply, storage, and transport at shield-stage Hawaiian volcanoes, in *Characteristics of Hawaiian Volcanoes*, edited by M. P. Poland, *U.S. Geol. Surv. Prof. Pap., 1801*, 1–52.
Rowan, L., and R. W. Clayton (1993), The three-dimensional structure of Kilauea Volcano, Hawaii, from travel time tomography, *J. Geophys. Res.*, *98*, 4355–4375.
Rubin, A., D. Gillard, and J. Got (1998), A reinterpretation of seismicity associated with the January 1983 dike intrusion at Kilauea Volcano, Hawaii, *J. Geophys. Res.*, *103*, 10,003–10,015.
Ryall, A., and D. L. Bennett (1968), Crustal structure of southern Hawaii related to volcanic processes in the upper mantle, *J. Geophys. Res.*, *73*, 4561–4582.
Shillington, D. J., H. J. A. Van Avendonk, M. D. Behn, P. B. Kelemen, and O. Jagoutz (2013), Constraints on the composition of the Aleutian arc lower crust from Vp/Vs, *Geophys. Res. Lett.*, *40*, 2579–2584, doi:10.1002/grl.50375.
Spakman, W., and H. Bijwaard (2001), Optimization of cell parameterizations for tomographic inverse problems, *Pure Appl. Geophys.*, *158*, 1401–1423.
Spencer, C., and D. Gubbins (1980), Travel-time inversion for simultaneous earthquake location and velocity structure determination in laterally varying media, *Geophys. J. R. Astron. Soc.*, *63*, 95–116.
Swanson, D., W. Duffield, and R. Fiske (1976), Displacement of the south flank of Kilauea Volcano: The result of forceful intrusion of magma into the rift zones, *U.S. Geol. Surv. Prof. Pap.*, *963*, 1–39.
Syracuse, E. M., C. H. Thurber, C. J. Wolfe, P. G. Okubo, J. H. Foster, and B. A. Brooks (2010), High-resolution locations of triggered earthquakes and tomographic imaging of Kilauea Volcano's south flank, *J. Geophys. Res.*, *115*, B10310, doi:10.1029/2010JB007554.
Thurber, C. (1984), Seismic detection of the summit magma complex of Kilauea volcano, Hawaii, *Science*, *223*, 165–167.
Thurber, C., and D. Eberhart-Phillips (1999), Local earthquake tomography with flexible gridding, *Comput. Geosci.*, *25*, 809–818.
Thurber, C. H. (1983), Earthquake locations and three-dimensional crustal structure in the Coyote Lake area, central California, *J. Geophys. Res.*, *88*, 8226–8236.
Thurber, C. H. (1987), Seismic structure and tectonics of Kilauea Volcano, *U.S. Geol. Surv. Prof. Pap.*, *1350*, 919–934.
Thurber, C. H. (1993), Local earthquake tomography: Velocities and Vp/Vs-theory, in *Seismic Tomography: Theory and Practice*, edited by H. M. Iyer and K. Hirahara, pp. 563–583, Chapman and Hall, London, U. K.
Zucca, J. J., and D. P. Hill (1980), Crustal structure of the southeast flank of Kilauea Volcano, Hawaii, from seismic refraction measurements, *Bull. Seismol. Soc. Am.*, *70*, 1149–1159.